



Deposited via The University of Sheffield.

White Rose Research Online URL for this paper:

<https://eprints.whiterose.ac.uk/id/eprint/232362/>

Version: Published Version

---

**Article:**

Durney, C.H., Wilson, M.J., McGregor, S. et al. (2023) Grasses exploit geometry to achieve improved guard cell dynamics. *Current Biology*, 33 (13). 2814-2822.e4. ISSN: 0960-9822

<https://doi.org/10.1016/j.cub.2023.05.051>

---

**Reuse**

This article is distributed under the terms of the Creative Commons Attribution (CC BY) licence. This licence allows you to distribute, remix, tweak, and build upon the work, even commercially, as long as you credit the authors for the original work. More information and the full terms of the licence here:

<https://creativecommons.org/licenses/>

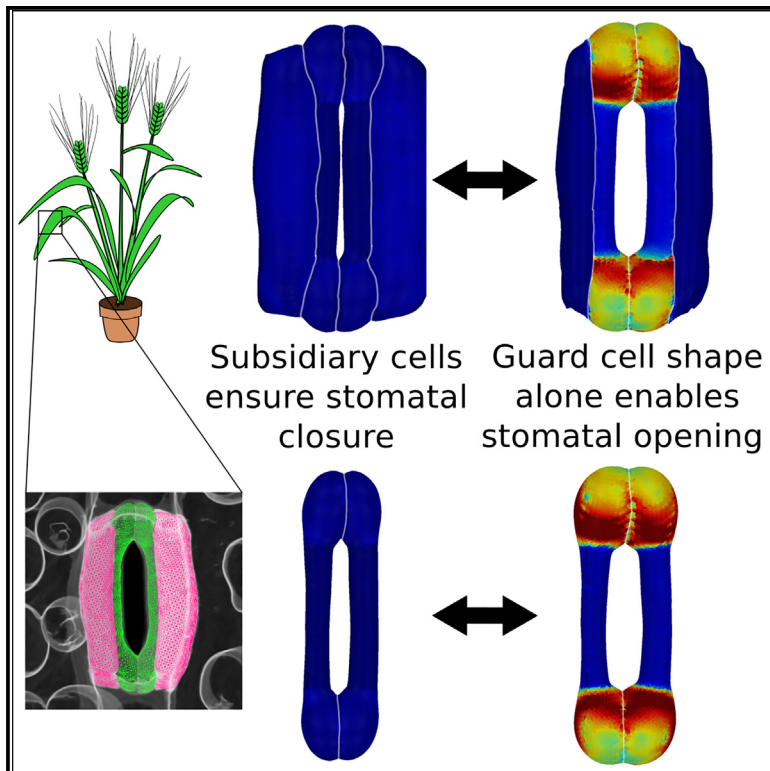
**Takedown**

If you consider content in White Rose Research Online to be in breach of UK law, please notify us by emailing [eprints@whiterose.ac.uk](mailto:eprints@whiterose.ac.uk) including the URL of the record and the reason for the withdrawal request.

# Current Biology

## Grasses exploit geometry to achieve improved guard cell dynamics

### Graphical abstract



### Authors

Clinton H. Durney, Matthew J. Wilson, Shauni McGregor, ..., Julie E. Gray, Richard J. Morris, Andrew J. Fleming

### Correspondence

richard.morris@jic.ac.uk (R.J.M.), a.fleming@sheffield.ac.uk (A.J.F.)

### In brief

Grasses have a specialized form of stomata, which leads to enhanced water-use efficiency. Via computational and experimental approaches, Durney et al. show that cellular geometry sets the mechanics required for effective pore closure. The results indicate that acquisition of specific cell shape was core to the evolutionary success of our major crops.

### Highlights

- Computational modeling captures the performance of grass stomata
- Specialized guard and subsidiary cell shapes set system mechanics
- Normal stomatal function needs a thick guard cell rod but not wall anisotropy
- Full pore closure in grasses mechanically requires subsidiary cells



Report

# Grasses exploit geometry to achieve improved guard cell dynamics

Clinton H. Durney,<sup>1,3</sup> Matthew J. Wilson,<sup>2,3</sup> Shauni McGregor,<sup>2</sup> Jodie Armand,<sup>2</sup> Richard S. Smith,<sup>1</sup> Julie E. Gray,<sup>2</sup> Richard J. Morris,<sup>1,\*</sup> and Andrew J. Fleming<sup>2,4,\*</sup>

<sup>1</sup>Computational and Systems Biology, John Innes Centre, Norwich Research Park, Norwich NR4 7UH, UK

<sup>2</sup>Plants, Photosynthesis and Soils, School of Biosciences, University of Sheffield, Western Bank, Sheffield S10 2TN, UK

<sup>3</sup>These authors contributed equally

<sup>4</sup>Lead contact

\*Correspondence: richard.morris@jic.ac.uk (R.J.M.), a.fleming@sheffield.ac.uk (A.J.F.)

<https://doi.org/10.1016/j.cub.2023.05.051>

## SUMMARY

Stomata are controllable micropores formed between two adjacent guard cells (GCs) that regulate gas flow across the plant surface.<sup>1</sup> Grasses, among the most successful organisms on the planet and the main food crops for humanity, have GCs flanked by specialized lateral subsidiary cells (SCs).<sup>2–4</sup> SCs improve performance by acting as a local pool of ions and metabolites to drive changes in turgor pressure within the GCs that open/close the stomatal pore.<sup>4–8</sup> The 4-celled complex also involves distinctive changes in geometry, having dumbbell-shaped GCs compared with typical kidney-shaped stomata.<sup>2,4,9</sup> However, the degree to which this distinctive geometry contributes to improved stomatal performance, and the underlying mechanism, remains unclear. To address this question, we created a finite element method (FEM) model of a grass stomatal complex that successfully captures experimentally observed pore opening/closure. Exploration of the model, including *in silico* and experimental mutant analyses, supports the importance of a reciprocal pressure system between GCs and SCs for effective stomatal function, with SCs functioning as springs to restrain lateral GC movement. Our results show that SCs are not essential but lead to a more responsive system. In addition, we show that GC wall anisotropy is not required for grass stomatal function (in contrast to kidney-shaped GCs<sup>10</sup>) but that a relatively thick GC rod region is needed to enhance pore opening. Our results demonstrate that a specific cellular geometry and associated mechanical properties are required for the effective functioning of grass stomata.

## RESULTS AND DISCUSSION

### An FEM model of a grass stomate indicates that a reciprocal pressure system is required for optimum function

Stomata in barley, which show a classical dumbbell structure (Figure 1A), were induced to close with abscisic acid (ABA) or open with fusicoccin (Fc) and visualized via confocal light microscopy after staining (Figures S1A–S1D). We segmented the image stacks to reconstruct guard cells (GCs) and the adjacent subsidiary cells (SCs) (Figures 1B and 1C). Longitudinal slices (transect [i] in Figures 1B and 1D) revealed a distinct “bone” shape in which the GC bulbous ends expanded below the plane of the rod region and extended in the longitudinal axis to subtend the adjacent epidermal cells. This subtending of epidermal cells at the poles of the stomatal complex was also revealed in longitudinal views of the SCs (transect [ii] in Figures 1B and 1D). Cross-sections through the GC rod region (transect [iii] in Figures 1B and 1E) and bulbous ends (transect [iv] in Figures 1B and 1E) revealed differences in shape in closed stomata. Comparison of the cross-sections in Figure 1E with those in stomata treated with an opening stimulus (Figure 1F; transects [v] and [vi] in Figures 1C and 1F) highlighted the complex

changes in shape in the different regions of the GCs and SCs that occurred. We validated these differences via TEM of the mid-rod (Figure 1G) and bulbous end regions (Figure 1H). This allowed estimation of cell wall thickness, highlighting the extreme thickening of the GC wall in the rod region (Figure S1G). Analysis of the GC rod (Figure 1I) and bulbous ends (Figure 1J) showed that during stomatal opening a significant increase in volume was restricted to the bulbous ends. Because previous work on kidney-shaped GCs revealed that mechanical wall anisotropy was required for stomatal function,<sup>10–12</sup> we analyzed this parameter in barley. The results showed that in closed and open GCs the cell wall was anisotropic, with a preferential orientation along the long axis of the rod region (Figures 1K, 1L, S1E, and S1F). A consensus pattern of wall anisotropy is depicted in Figure 1M, which is comparable to patterns reported in other grass stomata and which likely reflects the orientation of cellulose microfibrils.<sup>13,14</sup>

The data from confocal imaging, together with the analysis of wall thickness and anisotropy, as well as data from the literature (Table S1), were used to parameterize a finite element method (FEM) model of the barley stomatal complex. It is well established that during stomatal opening the internal turgor pressure of GCs increases, leading to an increase in pore aperture.<sup>1,4</sup>



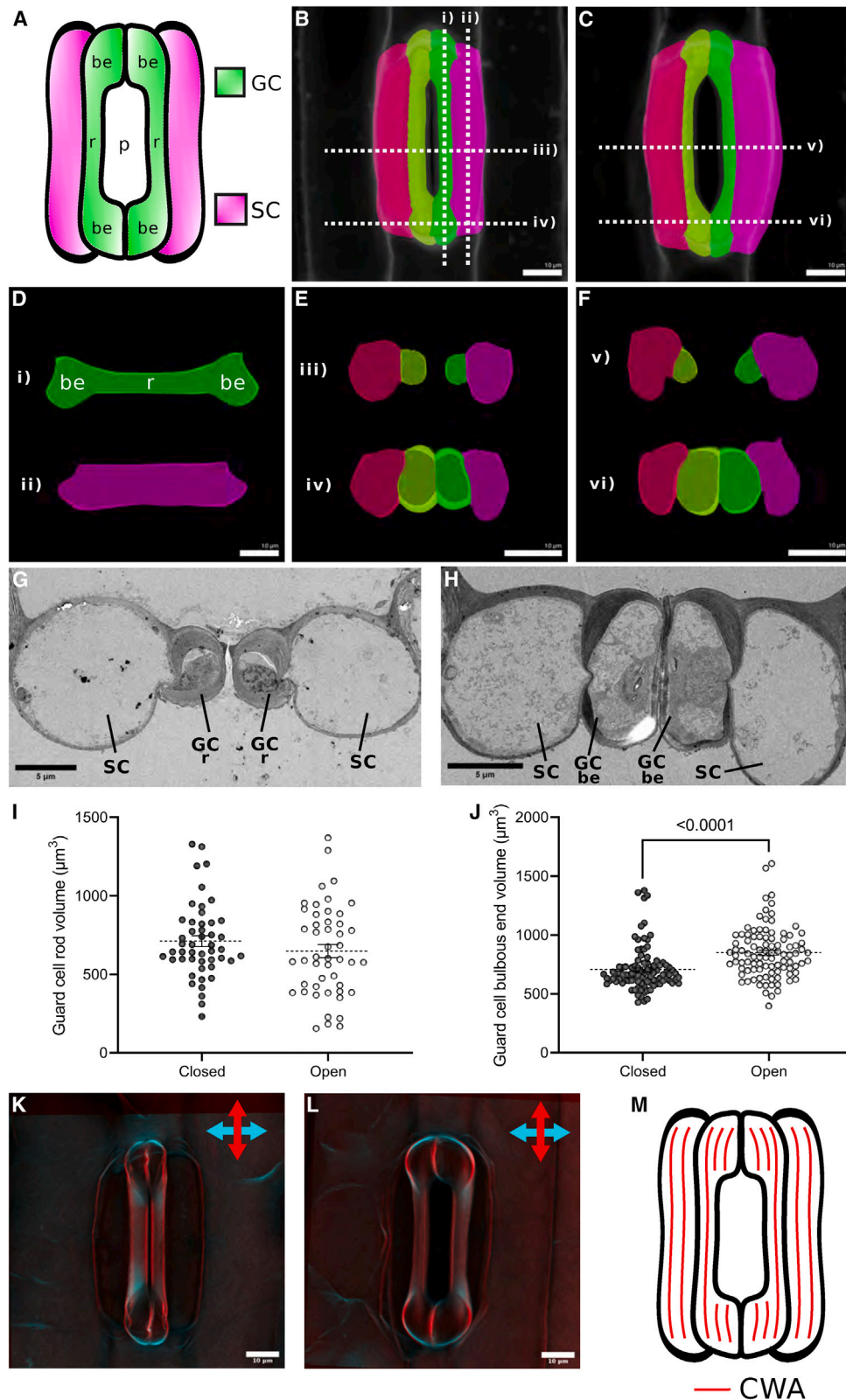


**Figure 1. Imaging of barley stomata reveals shape changes in guard and subsidiary cells during pore opening**

(A) Schematic of a barley stomatal complex composed of guard cells (green) and subsidiary cells (magenta). The guard cells are distinguished by bulbous ends (be) connected by a rod region (r), as indicated, which surround the stomatal pore (p).

(legend continued on next page)

With respect to the concomitant pressure changes in the SCs, a number of possibilities exist. For example, SC pressure could remain constant and relatively low, constant and relatively high, or (as supported by the available experimental data<sup>9,15,16</sup>) there could be a reciprocal change so that as GC pressure increases, SC pressure decreases, and vice versa. We explored these possibilities using our FEM model with the parameters in [Tables S2](#) and [S3](#). When SC pressure was maintained at a constant, relatively high level ( $P = 0.7$  MPa) and GC pressure gradually raised from 0 to 5 MPa, pore aperture increased ([Figure 2A](#), blue line). When SC pressure was maintained at a constant, relatively low level (0.2 MPa) and GC pressure increased, pore aperture again increased, but the response curve was offset so that even at low GC pressure the pore aperture was large ([Figure 2A](#), red line). These results indicate that a change in SC pressure is not absolutely required for grass stomata to open. When a reciprocal GC/SC pressure system was implemented, a change in the pressure/aperture response curve was observed, with the rate of aperture opening per increase in GC turgor pressure being higher than in either of the static SC pressure simulations ([Figure 2A](#), black line). Furthermore, when the simulated change in pore area between closing and opening was compared with that measured experimentally, the reciprocal pressure model successfully captured observed stomatal behavior ([Figure 2G](#)).

A main output of an FEM model is the resulting stress/strain pattern. When closed, stress was uniform and low in both GCs and SCs ([Figure 2B](#)). As GC pressure was increased and SC pressure decreased (leading to pore opening), an increase in stress occurred, focused within the bulbous ends, with little increase in stress within the GC rod or SCs ([Figure 2C](#); [Video S1A](#)). A similar stress profile and aperture increase on stomatal opening was obtained when we implemented a 3D element simulation informed by the same parameters used for the FEM models in [Figure 2](#) ([Figures S1I](#) and [S1J](#)), indicating that the 2D element approach used was appropriate.

Taken together, our FEM model successfully captures the main elements of grass stomatal movement. The model supports the hypothesis that a reciprocal GC/SC pressure system is required for efficient functioning of grass stomata,<sup>15,16</sup> maximizing aperture response per change in unit volume. However, even without a reciprocal pressure system the grass GCs would still be able to open and close the stomatal pore. The presence of pressurized SCs has a mechanical influence on the system by restraining the size of the pore aperture when GC pressure is low, effectively acting as a spring to compress the GCs in a relaxed state.

### Combined *in silico* and experimental mutant analyses show that subsidiary cells are not required for grass stomatal function but enhance pore closure

To further investigate the role of SCs, we performed a digital ablation experiment in which the SCs were removed from our reciprocal pressure model. The results indicated that in the absence of SCs an increase in GC pressure still led to an increase in stomatal aperture; however, the pressure/aperture response curve was shifted, leading to a smaller change of aperture per change in GC pressure ([Figure 2D](#), compare yellow line to black line). The initial pore aperture in the relaxed isolated GCs was higher than in the intact reciprocal pressure model, indeed higher than in the model with constant high SC pressure (red line in [Figure 1A](#)). Similar to the intact reciprocal pressure model, stress changes during pore opening in the digitally isolated GCs were focused in the bulbous ends, with little change in the rod region ([Figures 2E](#) and [2F](#)). These results indicate that SCs are not absolutely required for grass stomatal function but are necessary for effective functioning. Without SCs, the stomatal aperture is predicted never to close, even when GC pressure is zero, supporting a direct mechanical role for SCs in restraining GC lateral movement.

To experimentally test the ideas on SC function raised by our digital ablation experiments, we turned to a genetic mutant, *bdmute*, which lacks SCs.<sup>17</sup> This mutant is in the grass *Brachypodium distachyon* (brachypodium), so we first developed an FEM model for stomatal complexes in this species to allow direct comparison with experimental data. Because our data showed that light/CO<sub>2</sub> was comparable to Fc as a trigger ([Figure S1H](#)), we used these to manipulate opening/closing of the brachypodium stomata. Confocal imaging of wild-type (WT) brachypodium allowed us to capture and segment 3D structures comprising GCs and SCs from stomata triggered to close or open ([Figure 3A](#)). Longitudinal slices through GCs in closed and open stomata ([Figure 3A](#)) revealed a similar yet distinct shape from those observed in barley, with GCs in brachypodium having relatively shorter rods and longer bulbous ends ([Figure S2](#)). When *bdmute* plants were analyzed, the lack of SCs was clear ([Figure 3B](#)), as reported.<sup>17</sup> Longitudinal transects revealed that the shape of these GCs was distinct from those in WT brachypodium ([Figure 3B](#), compare with [Figure 3A](#)), with the *bdmute* GCs being relatively shorter and deeper in the rod region and having relatively longer bulbous ends ([Figure S2](#)). These data, along with TEM of the stomata, analysis of wall anisotropy ([Figure S3](#)), and inferred Young's moduli ([Table S1](#)), were used to

(B and C) Confocal image stacks of stomata induced to close by ABA (B) or open by fusicoccin (C), rendered into 3D images comprising guard cells (green) and subsidiary cells (magenta). The plane of section used to obtain images in (D)–(F) is shown by dotted lines (i) to (vi) in (B) and (C).

(D) Longitudinal transect through a guard cell (green) (plane [i] in B) and a subsidiary cell (magenta) (plane [ii] in B).

(E and F) Cross-sections through closed (E) and open (F) stomata taken at planes (iii) and (iv) in (B) for closed stomata and planes (v) and (vi) in (C) for open stomata.

(G and H) TEM cross-sections of closed stomata taken either in the rod region (G) or bulbous end region (H).

(I and J) Volumes of the guard cell rod region (I) and bulbous ends (J) in stomata induced to either close with ABA or open with fusicoccin, as indicated. Data points indicate individual cells, with horizontal lines indicating mean values and bars indicating SEM. Statistical analysis indicated that the rod region volumes could not be distinguished from each other (unpaired t test,  $t(94) = 1.179$ ,  $p = 0.2415$ ,  $n = 48$ ), whereas the bulbous end volumes for ABA and Fc-treated samples were different (unpaired t test with Welch's correction,  $t(186.2) = 4.881$ ,  $p \leq 0.0001$ ,  $n = 96$ ).

(K and L) Analysis of cellulose orientation in closed (K) and open (L) stomata revealed anisotropy in the cell walls, with the inference that fibrils are oriented predominantly along the long axis of the GCs (red signal), with transverse orientation (cyan signal) limited to the end walls of the bulbous ends.

(M) A schematic of the cell wall anisotropy (CWA) shown in (L) and (M) that was used to inform the FEM model of barley stomata.

Scale bars, 10  $\mu\text{m}$  (B–F, K, and L) and 5  $\mu\text{m}$  (G and H).

See also [Figure S1](#) and [Tables S1–S3](#).

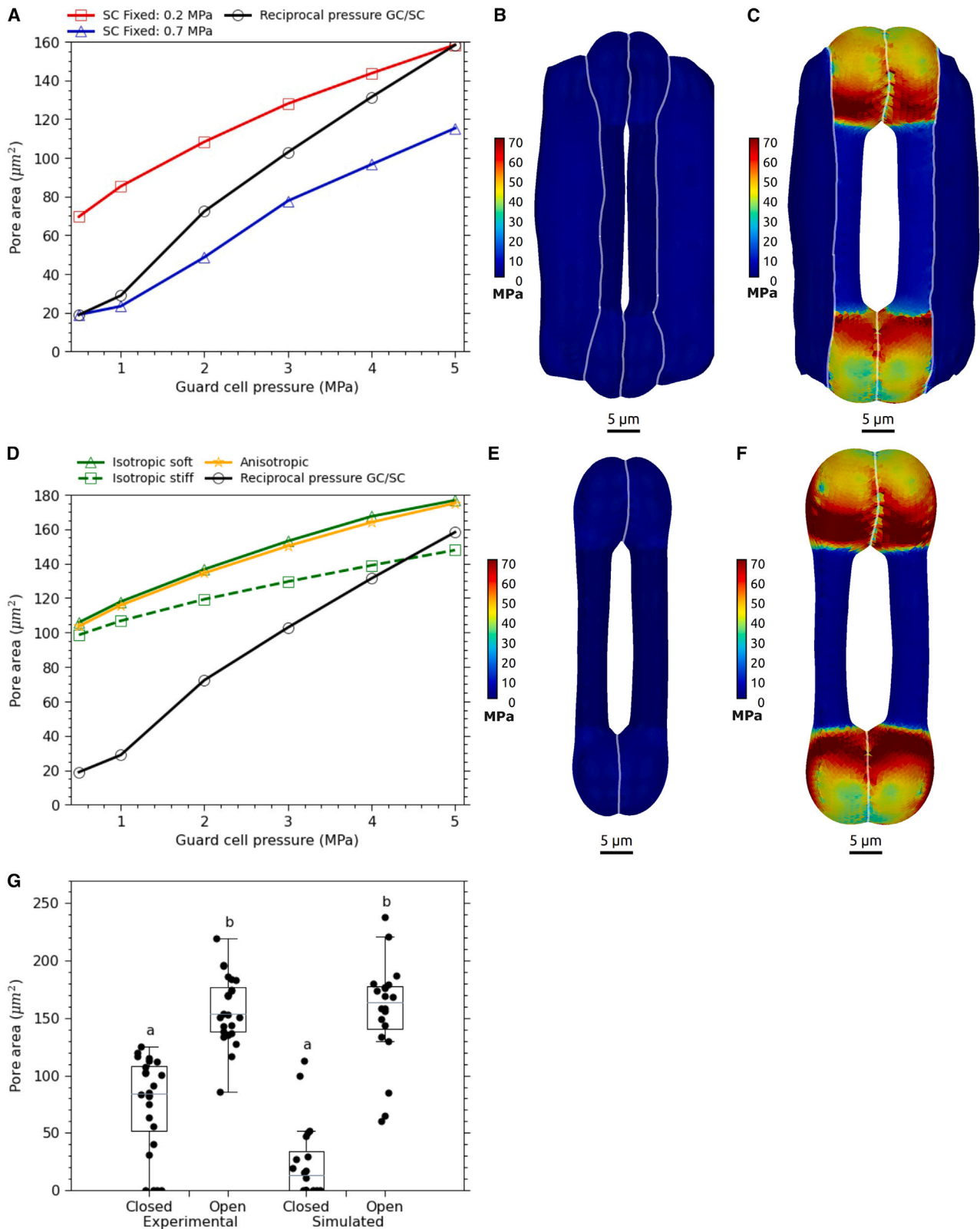


**Figure 2. An FEM model of a grass stomatal complex successfully captures pore opening and closure**

(A) Pore aperture/guard cell pressure relationships for a barley stomatal FEM model in which there is a reciprocal pressure relationship between GCs and SCs (black line) or in which SC pressure is fixed at a relatively low level (0.2 MPa, red line) or high level (0.7 MPa, blue line) as GC pressure is increased.

(legend continued on next page)

generate brachypodium stomate FEM models for WT and *bdmute*.

When the WT brachypodium FEM model was inflated using a reciprocal pressure system, pore aperture increased and the values predicted by the model reflected those observed in WT experimental samples induced to open (Figure 3C; Video S1B). When opening of the *bdmute* FEM model was simulated via increasing GC pressure, the stomatal pore aperture increased only slightly, similar to experimental observation (Figure 3D; Video S1C). We also performed a digital ablation on the WT brachypodium FEM model to remove the SCs, leaving only the isolated GCs. When these were inflated by increasing GC pressure, the aperture/pressure response curve was shifted relative to the WT brachypodium data, with the pore remaining wide open even at low GC pressure (Figure 3E). The aperture/pressure response curves for both the *bdmute* and isolated GC models showed shallower gradients than the intact WT reciprocal pressure model (Figure 3E, black line).

These results provide further evidence that loss of SCs leads to a diminished efficiency of stomatal opening (as measured by pressure/aperture response) but that some degree of movement is still possible.<sup>17</sup> In the digitally ablated brachypodium there was a relatively large pore in the relaxed state of the FEM model, supporting the idea that the SCs act as a spring to restrain pore opening at low GC pressures. Interestingly, the shape of the GCs in the *bdmute* mutant was different from that predicted simply by digital ablation of the WT SC (Figure S2). We speculate that this shift in geometry underpins the altered pressure/aperture response curves observed, further demonstrating the importance of GC geometry in the function of grass stomata.

### Differential wall thickness in the GC rod is needed for effective stomatal opening, but wall anisotropy is not

Our previous work using FEM models of kidney-shaped stomata suggested that radial organization of cellulose microfibrils, thus wall anisotropy, is essential for stomatal function.<sup>10</sup> Given our observations on grass stomata (Figures 1K–1M and S3C), we explored our FEM models to investigate the requirement of material anisotropy for pore opening/closure. When the cell wall material properties were adjusted to be isotropic and relatively soft in the barley FEM model and the meshes inflated using the

reciprocal pressure system, there was little change in the pressure/aperture response curve compared with the anisotropic model (Figure 4A, black versus green line). When the stiffness of the isotropic wall was increased (Figure 4A, green dotted line) the aperture/pressure response curve revealed a lower maximal aperture. Thus, although wall material properties did influence model behavior, wall anisotropy was not essential. Even when wall anisotropy was set in an orientation orthogonal to that observed in grass GCs (equivalent to the microfibrils being circumferentially oriented around the GCs, as in eudicots), function was not dissimilar to that observed in normal grass stomata (Figure 4A, yellow line). These results were consistent with data from the digitally ablated barley stomatal FEM model. With relatively soft isotropic walls the aperture/pressure response curve of the isolated GCs was very similar to the FEM model with anisotropic walls (Figure 2D, green versus yellow line). Stiffer isotropic GC walls led to a shift of the aperture/pressure response curve downward (Figure 2D, green dotted line). In all cases, after digital ablation of SCs the pore aperture remained large at low GC pressure. A similar picture emerged when we explored the outcome of loss or switching of direction of wall anisotropy in FEM models for WT brachypodium (Figure S4A) and *bdmute* (Figure S4N). In both cases, introduction of an isotropic rather than an anisotropic wall had minimal outcome on model performance (black versus green line), with wall stiffness modulating the pore aperture/pressure response curve.

These data indicate that wall anisotropy is not essential for the functioning of grass stomata. However, when the pattern of stress in the barley GCs was visualized for the different variants of wall isotropy/anisotropy described in Figure 4A, distinct patterns were observed in the bulbous ends. With a longitudinal anisotropy (as observed experimentally), maximal stress was predicted toward the base of the bulbous ends on the outer epidermal face (Figure 4B), focused on the tips of the bulbous ends when viewed end-on (Figure 4F). When the walls were implemented with isotropic properties, the stress pattern in the bulbous ends was similar to that observed in Figures 4B and 4F but displayed a decreased stress intensity in the outer epidermal face (Figures 4C and 4D) and a narrower focus of stress across a band in an end view of the stomate (Figures 4G and 4H), depending on wall stiffness (compare Figures 4C and

(B and C) Predicted stress patterns in the barley stomatal FEM model under low turgor pressure in the GCs (0.5 MPa) and high turgor pressure in the SCs (0.7 MPa) (B) and high GC pressure (5.0 MPa) and low SC pressure (0.2 MPa) (C). In (B), there is a low, approximately uniform stress pattern in all cells and a small pore aperture. At high GC pressure (C), pore aperture increases and a relatively high stress pattern occurs, but restricted to the bulbous ends.

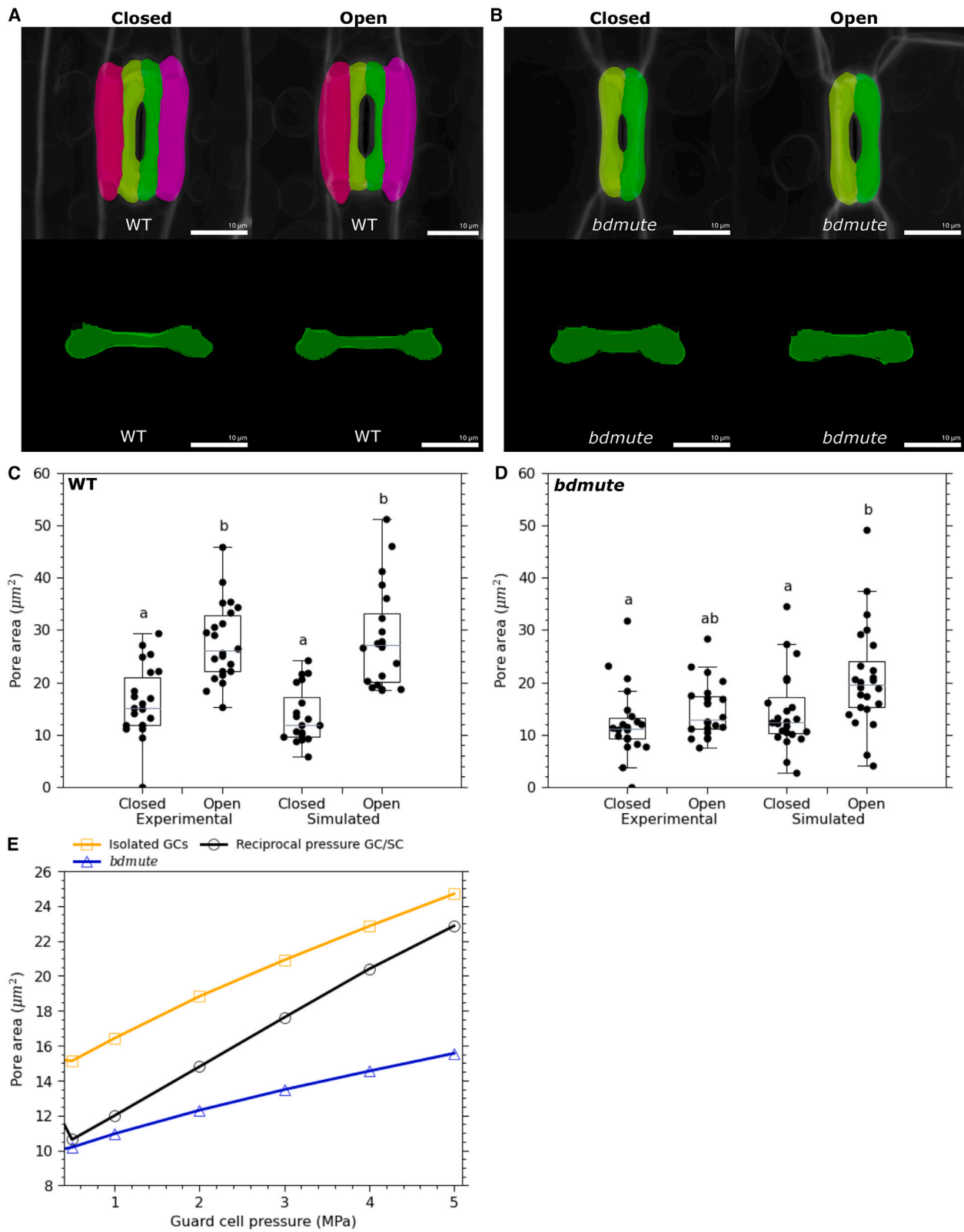
(D) Pore aperture/guard cell pressure relationships for a barley stomatal FEM model in which the SCs have been digitally ablated, leaving the isolated GCs. With cellulose anisotropy maintained as in the original FEM model, pore aperture increases as GC pressure increases (yellow line) but the initial pore aperture at low GC pressure is larger than that in the intact reciprocal pressure FEM model (response curve in black, as shown in A). When anisotropy is removed from the isolated GCs and stiffness set at a relatively low level in the FEM model, the aperture/pressure response curve is similar to that observed with anisotropy present (green line). As GC wall stiffness is increased in the isolated GCs, the aperture/pressure response curve shifts downward, with pore aperture remaining large at low GC pressure (dotted green line).

(E and F) Stress patterns in isolated GCs in either (E) resting state (low pressure) or (F) inflated state (high pressure). High stress is observed in the bulbous ends.

(G) Comparison of experimental and simulated pore aperture response in stomata induced to open or close via Fc or ABA (experimental) or the extremes of the intact reciprocal pressure model shown in (D) (simulated). Points indicate individual stomata for experimentally measured data and individual models derived from independently derived FEMs for simulated data. Horizontal lines indicate median values, with box plots indicating the range of the 25<sup>th</sup>–75<sup>th</sup> percentile. Pore area was significantly greater in open compared with closed stomata in both cases (Kruskal-Wallis,  $H = 60.85$ ,  $n = 24, 24, 20$ , and  $20$ ;  $p \leq 0.0001$ ), but it was not possible to distinguish experimental and simulated data following Dunn's multiple comparisons test ( $p \leq 0.05$ ), with letters indicating samples that cannot be distinguished from each other.

Scale bars, 5  $\mu\text{m}$  (B, C, E, and F), and intensity scales in (B), (C), (E), and (F) indicate predicted stress (MPa).

See also Figures S1 and S2, Tables S1–S3, and Video S1A.



(legend on next page)

4D). When the stress patterns in the bulbous ends of the brachypodium models (both WT and *bdmute*) were analyzed (Figures S4B–S4I and S4O–S4V, respectively), there was also a higher stress toward the base of the bulbous ends which was modulated by wall stiffness (Figures S4B–S4D and S4O–S4Q). However, the stress patterns observed in end-on views of the brachypodium FEM models (Figures S4F–S4I and S4S–S4V) were distinct from those observed in barley (Figures 4F–4I). The functional significance of these different stress patterns awaits elucidation but probably reflects slight differences in GC shape (Figure S2).

A geometrically distinguishing feature of grass GCs is the presence of the rod with a relatively thick cell wall<sup>18</sup> (Figure 1G). To explore the importance of this feature, we simulated the barley reciprocal pressure model with a range of rod wall thickness (with unchanged material properties and anisotropy from WT). The results showed that at rod wall thicknesses 3× or greater than that at the bulbous ends, there was little change in pore aperture/pressure response from those experimentally observed (Figure 4J). However, when rod wall thickness was decreased to be the same as the rest of the GC (1×, dotted line in Figure 4J), there was a shift in the pore aperture/pressure response curve, leading to a lag in pore opening as GC pressure increased. Moreover, when stress patterns were visualized in the relevant FEM models, a non-uniform stress pattern developed in the rod (Figure 4K). In contrast, when the rod wall thickness was set at 3× or higher than the bulbous end wall, the rods showed a uniform pattern of low stress (Figures 4L and 4M). A similar phenomenon was observed in the FEM models for WT brachypodium and *bdmute* (Figures S4J–S4M and S4W–S4Z, respectively). In both models, there was an offset in the aperture/pressure response curve once the relative rod wall thickness was decreased below 3, accompanied by the emergence of a non-uniform pattern and lower stress in the rod region.

Our data support the hypothesis that the rod region of grass stomata acts as an unextendible mechanical beam connecting the two bulbous ends, where localized volume changes drive stomatal opening by pushing apart the adjacent rods. A minimum stiffness is required in the rod, below which aberrant stress/strain patterns and opening behaviors emerge. Interestingly, the modeled minimum relative rod thickness required for effective stomatal function appears close to that observed experimentally.

The significance and mechanistic link of cellular geometry to plant function is being resolved.<sup>19–21</sup> Our results extend this work by providing insight into the importance of cellular geometry in grass stomata function. SCs function not only as a local pool of ions/metabolites to allow the reciprocal pressure system required for efficient opening/closure of the stomatal pore but also play a mechanical role in ensuring pore closure at low GC turgor pressure. These synergistic but distinct roles of SCs allow us to speculate that the morphological and biochemical transport adaptations required for effective grass stomatal function do not need to have evolved in parallel. The localization of volume changes to the bulbous ends allows a more pronounced response to relatively small absolute changes in cell volume but is dependent on the rod region being able to withstand stress. This is not achieved by anisotropy in the wall (as in kidney-shaped stomata) but by development of a relatively thick rod wall within a specialized cell shape. We propose that the unique geometry of the grass GCs and SCs plays a key role in their function by facilitating more effective opening and closure of the stomatal pore, underpinning one of the major evolutionary traits to improve water-use efficiency in our major crop species.

## STAR★METHODS

Detailed methods are provided in the online version of this paper and include the following:

- KEY RESOURCES TABLE
- RESOURCE AVAILABILITY
  - Lead contact
  - Materials availability
  - Data and code availability
- EXPERIMENTAL MODEL AND STUDY PARTICIPANT DETAILS
- METHOD DETAILS
  - Tissue treatments for stomatal opening and closing
  - Confocal imaging and segmentation
  - Transmission electron microscopy
  - Cell wall anisotropy
  - Stomatal measurements
  - Computational modelling
- QUANTIFICATION AND STATISTICAL ANALYSIS

### Figure 3. Modeling and experimental analysis of a stomatal mutant indicates a role for subsidiary cells in mechanically restraining pore aperture

(A and B) Stomatal complex cell shapes in (A) WT brachypodium or (B) *bdmute* leaves induced to close (darkness) or open (exposure to light), as indicated. Subsidiary cells (magenta) are adjacent to guard cells (green). Scale bars, 10 μm.

(C) Comparison of experimental and simulated pore aperture response in WT stomata induced to open or close via light or dark treatments (experimental) or the extremes of the reciprocal pressure model (simulated). Points indicate individual stomata for experimentally measured data and individual models derived from independently derived FEMs for simulated data. Horizontal lines indicate median values, with box plots indicating the range of the 25<sup>th</sup>–75<sup>th</sup> percentiles. Pore area was significantly greater in open compared with closed stomata in both cases (Kruskal-Wallis,  $H = 41.86$ ,  $n = 22, 22, 20$ , and  $20$ ;  $p \leq 0.0001$ ), but it was not possible to distinguish experimental and simulated data following Dunn's multiple comparisons test ( $p \leq 0.05$ ), with letters indicating samples that cannot be distinguished from each other.

(D) As in (C) but for experimental and simulated *bdmute* stomata. Pore area was significantly greater in simulated open stomata compared with simulated closed stomata (Kruskal-Wallis,  $H = 15.13$ ,  $n = 23, 22, 24$ , and  $24$ ;  $p = 0.017$ ), but it was not possible to distinguish experimental and simulated data following Dunn's multiple comparisons test ( $p \leq 0.05$ ), with letters indicating samples that cannot be distinguished from each other.

(E) Pore aperture/pressure response curves for WT brachypodium (black line), *bdmute* (blue line), and the isolated GCs after digital ablation of the SCs from the WT FEM model (yellow line).

See also Figures S2 and S3, Tables S1 and S2, and Videos S1B and S1C.

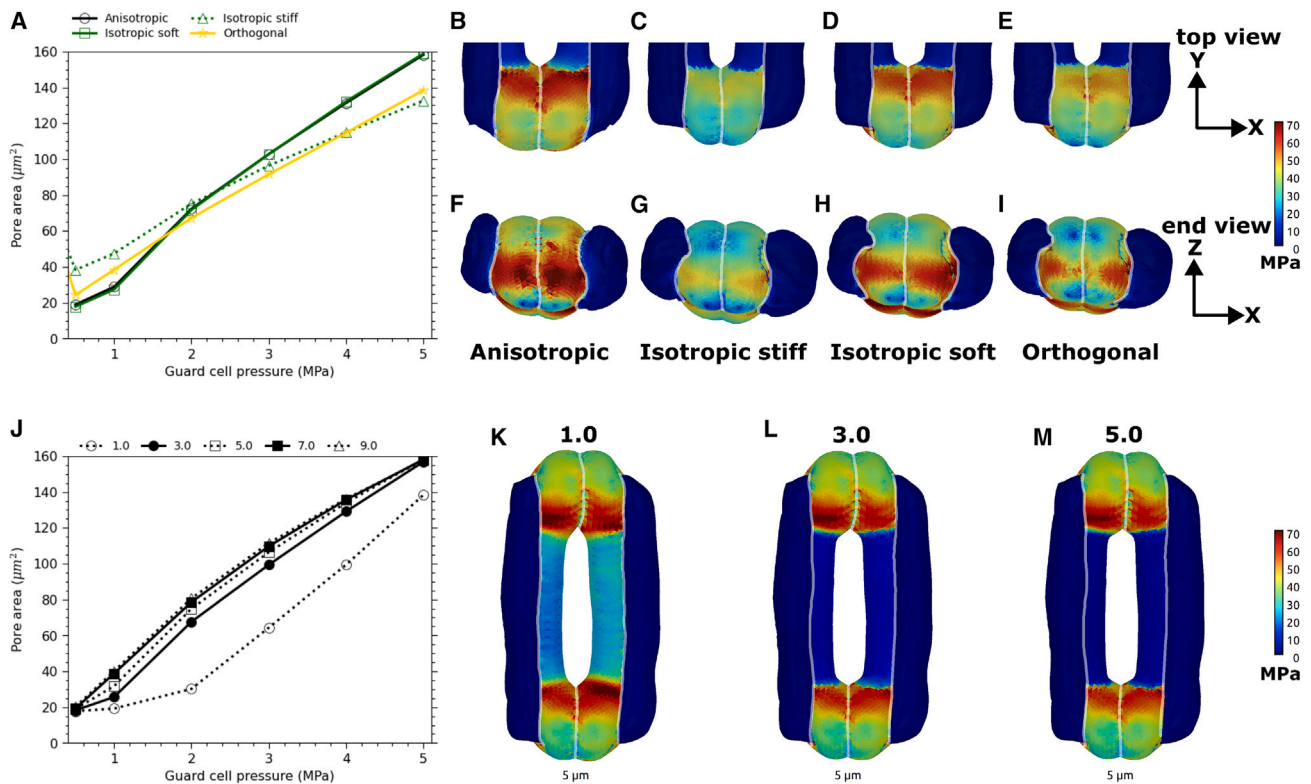


**Figure 4. Wall anisotropy is not required for grass stomatal opening, but a relatively thick rod wall is needed for effective stomatal function** (A) Pore aperture/GC pressure response curves for barley stomatal FEM models in which the GC wall is anisotropic (black line), isotropic and relatively soft (green line), or stiff (green dotted line), or in which wall anisotropy is orthogonal to that experimentally observed (yellow).

(B–E) Stress patterns in bulbous ends viewed in the outer epidermal plane for guard cells in which the wall is set to be (B) anisotropic, (C) isotropic and relatively stiff, (D) isotropic and relatively soft, and (E) orthogonal to the pattern observed experimentally.

(F–I) The same bulbous ends as (B)–(E) but viewed end-on along the epidermal plane.

(J) Pore aperture/GC pressure response curves for FEM models of WT barley stomata in which the thickness of the rod region wall of the GCs is set at a ratio to that in the bulbous ends of 1 $\times$  (open circle, dotted black line), 3 $\times$  (filled circle, solid black line), 5 $\times$  (open square, dotted black line), 7 $\times$  (filled square, dotted black line), or 9 $\times$  (open triangle, dotted black line).

(K–M) Stress patterns in barley stomatal FEM models in which the thickness of the rod region wall of the GCs is set at a ratio of (K) 1 $\times$ , (L) 3 $\times$ , and (M) 5 $\times$  to that in the bulbous ends.

Scale bars, 5  $\mu\text{m}$  (K–M), and intensity scales in (B)–(I) and (K)–(M) indicate predicted stress (MPa).

See also Figure S4.

#### SUPPLEMENTAL INFORMATION

Supplemental information can be found online at <https://doi.org/10.1016/j.cub.2023.05.051>.

#### ACKNOWLEDGMENTS

A.J.F., J.E.G., R.J.M., R.S.S., M.J.W., and C.H.D. acknowledge support by BBSRC grant “Shape Shifting Stomata: The Role of Geometry in Plant Cell Function” (BB/T005041), with further support via BBSRC’s Institute Strategic Programme “Plant Health” BB/P012574/1 to R.J.M. and BB/P013511/1 to R.S.S., and a BBSRC-White Rose DTP (BB/M011151) studentship to J.A. (A.J.F./J.E.G.). *bdmute* was kindly provided by Michael Raissig (University of Bern, Switzerland). Imaging was performed at the Wolfson Light Microscope Facility at the University of Sheffield.

#### AUTHOR CONTRIBUTIONS

Conceptualization, A.J.F., R.J.M., and J.E.G.; investigation, C.H.D., M.J.W., S.M., J.A., and R.S.S.; writing – original draft, A.J.F. with contributions from

all authors; writing – review & editing, all authors; supervision, A.J.F., J.E.G., R.J.M., and R.S.S.; funding acquisition, A.J.F., J.E.G., R.J.M., and R.S.S.

#### DECLARATION OF INTERESTS

The authors declare no competing interests.

#### INCLUSION AND DIVERSITY

We support inclusive, diverse, and equitable conduct of research.

Received: February 10, 2023

Revised: April 27, 2023

Accepted: May 23, 2023

Published: June 15, 2023

#### REFERENCES

- Hetherington, A.M., and Woodward, F.I. (2003). The role of stomata in sensing and driving environmental change. *Nature* 424, 901–908.

2. Nunes, T.D.G., Zhang, D., and Raissig, M.T. (2020). Form, development and function of grass stomata. *Plant J.* *101*, 780–799.
3. Raissig, M.T., Abrash, E., Bettadapur, A., Vogel, J.P., and Bergmann, D.C. (2016). Grasses use an alternatively wired bHLH transcription factor network to establish stomatal identity. *Proc. Natl. Acad. Sci. USA* *113*, 8326–8331.
4. McKown, K.H., and Bergmann, D.C. (2018). Grass stomata. *Curr. Biol.* *28*, R814–R816.
5. McAusland, L., Vialet-Chabrand, S., Davey, P., Baker, N.R., Brendel, O., and Lawson, T. (2016). Effects of kinetics of light-induced stomatal responses on photosynthesis and water-use efficiency. *New Phytol.* *211*, 1209–1220.
6. Raschke, K., and Fellows, M.P. (1971). Stomatal movement in *Zea mays*: shuttle of potassium and chloride between guard cells and subsidiary cells. *Planta* *101*, 296–316.
7. Schäfer, N., Maierhofer, T., Herrmann, J., Jørgensen, M.E., Lind, C., von Meyer, K., Lautner, S., Fromm, J., Felder, M., Hetherington, A.M., et al. (2018). A tandem amino acid residue motif in guard cell SLAC1 anion channel of grasses allows for the control of stomatal aperture by nitrate. *Curr. Biol.* *28*, 1370–1379.e5.
8. Mumm, P., Wolf, T., Fromm, J., Roelfsema, M.R., and Marten, I. (2011). Cell type-specific regulation of ion channels within the maize stomatal complex. *Plant Cell Physiol.* *52*, 1365–1375.
9. Franks, P.J., and Farquhar, G.D. (2007). The mechanical diversity of stomata and its significance in gas-exchange control. *Plant Physiol.* *143*, 78–87.
10. Woolfenden, H.C., Bourdais, G., Kopschke, M., Miedes, E., Molina, A., Robatzek, S., and Morris, R.J. (2017). A computational approach for inferring the cell wall properties that govern guard cell dynamics. *Plant J.* *92*, 5–18.
11. Woolfenden, H.C., Baillie, A.L., Gray, J.E., Hobbs, J.K., Morris, R.J., and Fleming, A.J. (2018). Models and mechanisms of stomatal mechanics. *Trends Plant Sci.* *23*, 822–832.
12. Rui, Y., and Anderson, C.T. (2016). Functional analysis of cellulose and xyloglucan in the walls of stomatal guard cells of *Arabidopsis*. *Plant Physiol.* *170*, 1398–1419.
13. Shtein, I., Shelef, Y., Marom, Z., Zelinger, E., Schwartz, A., Popper, Z.A., Bar-On, B., and Harpaz-Saad, S. (2017). Stomatal cell wall composition: distinctive structural patterns associated with different phylogenetic groups. *Ann. Bot.* *119*, 1021–1033.
14. Spiegelhalter, R.P., and Raissig, M.T. (2021). Morphology made for movement: formation of diverse stomatal guard cells. *Curr. Opin. Plant Biol.* *63*, 102090.
15. Franks, P.J., Cowan, I.R., and Farquhar, G.D. (1998). A study of stomatal mechanics using the cell pressure probe. *Plant Cell Environ.* *21*, 94–100.
16. Franks, P.J., Buckley, T.N., Shope, J.C., and Mott, K.A. (2001). Guard cell volume and pressure measured concurrently by confocal microscopy and the cell pressure probe. *Plant Physiol.* *125*, 1577–1584.
17. Raissig, M.T., Matos, J.L., Anleu Gil, M.X., Kornfeld, A., Bettadapur, A., Abrash, E., Allison, H.R., Badgley, G., Vogel, J.P., Berry, J.A., et al. (2017). Mobile MUTE specifies subsidiary cells to build physiologically improved grass stomata. *Science* *355*, 1215–1218.
18. Wille, A.C., and Lucas, W.J. (1984). Ultrastructural and histochemical studies on guard cells. *Planta* *160*, 129–142.
19. Sapala, A., Runions, A., Routier-Kierzkowska, A.L., Das Gupta, M., Hong, L., Hofhuis, H., Verger, S., Mosca, G., Li, C.B., Hay, A., et al. (2018). Why plants make puzzle cells, and how their shape emerges. *eLife* *7*, e32794.
20. Coen, E., and Cosgrove, D.J. (2023). The mechanics of plant morphogenesis. *Science* *379*, eade8055.
21. Kierzkowski, D., and Routier-Kierzkowska, A.L. (2019). Cellular basis of growth in plants: geometry matters. *Curr. Opin. Plant Biol.* *47*, 56–63.
22. Schindelin, J., Rueden, C.T., Hiner, M.C., and Eliceiri, K.W. (2015). The ImageJ ecosystem: an open platform for biomedical image analysis. *Mol. Reprod. Dev.* *82*, 518–529.
23. Strauss, S., Runions, A., Lane, B., Eschweiler, D., Bajpai, N., Trozzi, N., Routier-Kierzkowska, A.L., Yoshida, S., Rodrigues da Silveira, S., Vijayan, A., et al. (2022). Using positional information to provide context for biological image analysis with MorphoGraphX 2.0. *eLife* *11*, e72601.
24. Hofhuis, H., Moulton, D., Lessinnes, T., Routier-Kierzkowska, A.L., Bompfrey, R.J., Mosca, G., Reinhardt, H., Sarchet, P., Gan, X., Tsiantis, M., et al. (2016). Morphomechanical innovation drives explosive seed dispersal. *Cell* *166*, 222–233.
25. Mosca, G., Sapala, A., Strauss, S., Routier-Kierzkowska, A.L., and Smith, R.S. (2017). On the micro-indentation of plant cells in a tissue context. *Phys. Biol.* *14*, 015003.
26. Wilson, M.J., Fradera-Soler, M., Summers, R., Sturrock, C.J., and Fleming, A.J. (2021). Ploidy influences wheat mesophyll cell geometry, packing and leaf function. *Plant Direct* *5*, e00314.
27. Vijayan, A., Tofanelli, R., Strauss, S., Cerrone, L., Wolny, A., Strohmeier, J., Kreshuk, A., Hamprecht, F.A., Smith, R.S., and Schneitz, K. (2021). A digital 3D reference atlas reveals cellular growth patterns shaping the *Arabidopsis* ovule. *eLife* *10*, e63262.
28. Fernandez, R., and Moisy, C. (2021). FijiYama: a registration tool for 3D multimodal time-lapse imaging. *Bioinformatics* *37*, 1482–1484.
29. Franks, P.J. (2004). Stomatal control and hydraulic conductance, with special reference to tall trees. *Tree Physiol.* *24*, 865–878.
30. Carter, R., Woolfenden, H., Baillie, A., Amsbury, S., Carroll, S., Healicon, E., Sovatzoglou, S., Braybrook, S., Gray, J.E., Hobbs, J., et al. (2017). Stomatal opening involves polar, not radial, stiffening of guard cells. *Curr. Biol.* *27*, 2974–2983.e2.

## STAR★METHODS

### KEY RESOURCES TABLE

REAGENT or RESOURCE	SOURCE	IDENTIFIER
<b>Chemicals, peptides, and recombinant proteins</b>		
Fusicoccin	Sigma-Aldrich	Cat#F0537
Abscisic acid	Sigma-Aldrich	Cat#A1049
Propidium iodide	Sigma-Aldrich	Cat#81845
Pontamine Fast Scarlet	Sigma-Aldrich	Cat#212490
Araldite CY212 resin	Agar Scientific	Cat#AGR1030
<b>Experimental models: Organisms/strains</b>		
<i>Hordeum vulgare</i> : Golden Promise	Lab stocks	Golden Promise
<i>Brachypodium distachyon</i> : Bd21-3	Lab stocks	Bd21-3
<i>Bdmute</i>	Michael Raissig; Raissig et al. <sup>17</sup>	<i>Bdmute</i>
<b>Software and algorithms</b>		
ImageJ (Fiji)	Schindelin et al. <sup>22</sup>	<a href="https://imagej.net/">https://imagej.net/</a>
MorphoGraphX (version 2.0)	Strauss et al. <sup>23</sup>	<a href="https://www.morphographx.org/">https://www.morphographx.org/</a>
MorphoMechanX	Hofhuis et al., <sup>24</sup> Mosca et al. <sup>25</sup>	<a href="https://www.morphomechanx.org/">https://www.morphomechanx.org/</a>
Inflation Models for MorphoMechanX	This study	<a href="https://doi.org/10.5281/zenodo.7930565">https://doi.org/10.5281/zenodo.7930565</a>

### RESOURCE AVAILABILITY

#### Lead contact

Further information and requests for resources and reagents should be directed to and will be fulfilled by the lead contact, Andrew Fleming ([a.fleming@sheffield.ac.uk](mailto:a.fleming@sheffield.ac.uk)).

#### Materials availability

All newly created material in this paper can be obtained by contacting the lead contact.

#### Data and code availability

- Microscopy data reported in this paper will be shared by the lead contact upon request.
- All of the scripts used to run these simulations, process the data and generate the graphs are publicly available at clintondurney/grass-stomata-geometry (<https://doi.org/10.5281/zenodo.7930565>)
- Any additional information required to reanalyze the data reported in this paper is available from the lead contact upon request.

### EXPERIMENTAL MODEL AND STUDY PARTICIPANT DETAILS

Barley seeds (*Hordeum vulgare*, c.v. Golden Promise) were sown in module trays containing a substrate of Levington M3 compost. Trays were covered with a propagator lid and transferred into a controlled environment growth chamber (Conviron, PGR15: 16 h light/8 h dark, 21°C/16°C, 400  $\mu\text{mol m}^{-2}\text{s}^{-1}$  PPFD, 60% relative humidity). After 7–9 days, the first leaf was fully expanded and seedlings were either harvested for experimental work or transplanted into 110x110x120mm pots containing M3 and perlite (3:1, v/v) plus 5g of solid slow-release fertilizer and kept well-watered.

Seeds of *Brachypodium distachyon* (Bd21-3, *bdmute*) were sown directly into 70x70x80mm pots containing a 3:1 (v/v) mix of M3 and perlite after stratification at 4°C for 3–5 days. Pots were placed into a controlled environment growth chamber (Conviron, PGR15: 16 h light/8 h dark, 21°C/16°C, 400  $\mu\text{mol m}^{-2}\text{s}^{-1}$  PPFD, 60% relative humidity) and kept well-watered throughout their growth period.

### METHOD DETAILS

#### Tissue treatments for stomatal opening and closing

For barley, once the fifth leaf had fully expanded, three sections around 1  $\text{cm}^2$  were excised from the middle region of the leaf blade and immediately incubated for 2 h at 21°C in buffers designed to stimulate stomatal opening and closure. Opening buffer consisted of

50mM KCl, 10mM MES, 5mM KNO<sub>3</sub>, pH6.2 + 10 μM of fusicoccin (Fc), whilst the closing buffer had the same constituents except the Fc was replaced with 10 μM abscisic acid (ABA).

For *Brachypodium distachyon*, three sections were cut from the fully expanded fifth leaf and incubated in a buffer (50mM KCl, 10mM MES, 5mM KNO<sub>3</sub>, pH6.2) at 21°C and placed either in the light (400 μmol m<sup>-2</sup>s<sup>-1</sup>) supplied with air scrubbed of CO<sub>2</sub> using soda lime to induce stomatal opening or the dark under ambient CO<sub>2</sub> to close stomata.

After opening/closure treatments, leaf tissue from both grass species were immediately submerged in a fixative of 3:1 ethanol:acetic anhydride (v/v). Samples were vacuum infiltrated for 1 hour before being left in the fixative at 4°C for 48h. After this point, samples were rinsed in 50% ethanol before being transferred to 70% ethanol for storage.

### Confocal imaging and segmentation

Sample preparation for confocal laser scanning microscopy for both grass species was as described.<sup>26</sup> When samples were required for imaging, they were removed from 70% ethanol and briefly treated with absolute chloroform to remove epicuticular waxes. Samples were then progressively rehydrated via an ethanol series before samples were bleached and starch was removed via amylase treatment. Cell walls were stained with pseudo-schiff propidium iodide (PI) and samples were cleared in chloral hydrate+glycerol. Samples were mounted on slides in Hoyer's solution, covered with a coverslip and kept in the dark to avoid photobleaching. Samples were imaged within 3 days of mounting to avoid desiccation.

Images of individual barley stomata were collected using an Olympus FLUOVIEW FV1000 confocal system fitted with a 40x oil immersion objective (UPlanApo 40x, NA: 1.0). PI was excited using a 561 nm HeNe561 diode laser.<sup>26</sup> Scan resolution was 640 x 640 pixels with a pixel dwell time of 12 μs/pixel. No averaging was performed and bidirectional scanning was enabled. In order to aid segmentation accuracy, z-step was set 0.3 μm. Each stack began a few microns above the stomatal complex and ended a few microns below, in the substomatal cavity. 24 open and 24 closed stomata were imaged across 6 biological replicates for each treatment.

For brachypodium, images were collected using a Zeiss LSM800 AiryScan confocal microscope in LSM mode using a 20x air objective (Plan-Apochromat 20x, NA:0.8). Cell walls labelled with PI were visualized using the 561 laser and a 488/561 dichroic mirror. Resolution was set at 992 x 992 pixels and scan speed was set to maximum. Pinhole size was maintained at 1 AU. Step size was set at 0.3 μm, and each stack was initiated above, and completed below, each stomate. After images had been acquired, they were subjected to AiryScan Processing (Zen, Zeiss). A minimum of 22 individual stomata were imaged across 6 biological replicates for each treatment for both WT and mutant genotypes. Segmentation was performed using MorphoGraphX (MGX).<sup>23</sup> Images were first converted into.tiff files using FIJI,<sup>22</sup> and if required a gamma correction (value= 0.5) was applied before being imported into MGX. Contrast between cell boundaries and background was further improved using the "Stack/Filter/Brighten Darken" process in MGX. The strong fluorescent signal emitted by the stained cell wall in the thick rod region of the guard cell was normalized using a 3D UNet-based convolutional neural network (CNN) to predict cell boundaries prior to segmentation using the MGX process "Stack/CNN/UNet3D". Where required, the image was resampled during CNN processing to scale for voxel size. A difference-of-Gaussians filter (barley: radii of 0.3, 2μm; brachypodium: radii of 0.3, 0.5 μm) was applied to image stacks of stomata using the process "Stack/Filter/Diff Gaussians" to emphasize edges of the rod region, before the utilization of the built-in, pre-trained CNN for cell boundary prediction using the process "Stack/CNN/UNet3D"<sup>27</sup>. Stacks were then further blurred twice using the process "Stack/Filter/Gaussian Blur Stack" with a radius of 0.3 μm. Finally, segmentation of the processed 3D image was carried out using the "Stack/ITK/Segmentation/ITK Watershed Auto Seeded" function using a threshold of 500 for barley. This threshold was adjusted to 250 for brachypodium stacks. Since the watershed algorithm automatically identifies the mid-point, for relatively thick cell walls (e.g., in the rod region) the segmentation line is shifted slightly inwards from the true boundary (compare [Figures 1B](#) and [S1A](#)). Labels other than those corresponding to desired cells (i.e. epidermal pavement cells, mesophyll cells and intercellular air spaces) were manually removed from each stack, whilst any over-segmentation errors in the guard cells and subsidiary cells were corrected where required. Mesh files of cell geometry were generated using "Mesh/Creation/Marching Cubes 3D" with a cube size of 1 μm and 3 smooth passes. Where required to better capture cell geometry, meshes were smoothed further using the process "Mesh/Structure/Smooth Mesh". Mesh files were used directly to inform finite element analysis in MorphoMechanX. To explore geometry between cells, cell surface area and volume was extracted from the mesh using the process "Mesh/HeatMap/Heatmap Classic". Clipping planes in MGX were manipulated to produce longitudinal and transverse sections of individual cells and the complex respectively. In order to generate a mesh to extract bulbous end volume alone, the same process was followed minus running the boundary prediction steps. For each guard cell, guard cell rod volume was calculated as the sum of the bulbous end volume subtracted from the total guard cell volume.

### Transmission electron microscopy

5th fully expanded barley leaves were cut into 2mm by 5mm strips and fixed in 2% glutaraldehyde solution (v/v) in 0.1M sodium cacodylate buffer by vacuum infiltration. Tissue was then washed twice with PBS before secondary fixation with a 2% aqueous osmium tetroxide solution (v/v) for 2 h at room temperature. After another three washes with PBS, tissue was dehydrated with an ethanol series (30%, 50%, 70%, 90%, 100%, 100%, 30 min per change) and left in 100% ethanol overnight at room temperature. Samples were then transferred to propylene oxide for two changes, each for 15 min. Tissue was then infiltrated with Araldite CYC212 resin (Agar Scientific), (50% mixture of resin in propylene oxide, overnight; 100% resin, overnight). Tissue was then embedded in fresh resin and left to harden for 72 h at 60°C.

Ultrathin (70–90 nm) sections were taken with a Reichert-Jung Ultracut E ultramicrotome fitted with a DiATOME diamond knife and transferred to nickel grids. Sections were then stained with a 3% aqueous uranyl acetate solution for 30 min, de-stained with water for 30 min and then stained with Reynold's lead citrate for 5 min. Sections were then examined using an FEI Tecnai T12 Spirit Transmission Electron Microscope at an accelerating voltage of 80 kV. Electron micrographs were taken using a Gatan digital camera.

The total cell area and cytoplasm area were measured in ImageJ and the difference taken to give relative cell wall thickness. Stomata were measured from 6 different plants, giving a total n of at least 3 for the rod and bulbous end regions.

### Cell wall anisotropy

In barley, determination of wall anisotropy in stomata was carried out on the first fully expanded leaf (7–9 DAS). After excision, the abaxial epidermis of the leaf blade was isolated from the subtending mesophyll and adaxial epidermis via peeling. Whole leaf sections of leaf 5 were used for imaging of brachypodium cellulose orientation. Immediately after removal, the epidermis or leaf tissue was directly floated on a treatment buffer (50mM KCl, 10mM MES, 5mM KNO<sub>3</sub>, pH6.2) supplemented with either 10 μM Fc or 10 μM ABA to stimulate opening or closure respectively. Samples were incubated at 21°C in the light for 2 h, with the addition of the bifluorescent cellulose-specific stain 0.1% Pontamine Fast Scarlet (PFS) for the last 30 mins. After rinsing in 1x PBS, samples were mounted using treatment buffer in round glass-bottomed dishes.

Mounted samples were imaged using a Zeiss LSM800 AiryScan confocal microscope. Resolution was set at 992 x 992 pixels and scan speed was set to maximum. Pinhole size was maintained at 1 AU. Samples were oriented on the stage so that leaf vasculature (and thus stomatal long axis) was either aligned parallel or perpendicular to the polarization angle of the excitation beam. 3D z-stacks of individual stomata were collected, with a step size of 0.3 μm. After this first stack had been acquired, the sample was rotated by 90° on the stage and the process repeated. Each stomate was therefore imaged with the polarization angle of the laser both perpendicular and parallel to the long axis of the complex. In order to reduce any impacts of bleaching on the interpretation of fluorescence intensity data, the order in which stacks were taken was randomized. In barley, a total of 5 individual stomata were imaged for each of the buffer treatments, whereas 3 individual brachypodium stomata were imaged for each treatment in both WT and mutant genotypes.

Images were processed via AiryScan processing before being converted into.tiff files. Images of each of the orientations were initially approximately manually aligned before accurate computational 3D registration using the ImageJ plugin FijiYama.<sup>28</sup> Maximum intensity projections were produced in FIJI using aligned images.<sup>22</sup> Signal intensity differences resulting from the bifluorescent nature of PFS enabled gross patterns of cellulose microfibril orientation in guard cells and subsidiary cells to be observed.

### Stomatal measurements

Barley leaf tissue was excised from the plant and floated on buffer for 2h under 230 μmol m<sup>-2</sup> s<sup>-1</sup> (50mM KCl, 10mM MES, 5mM KNO<sub>3</sub>, pH6.2), with the addition of either 10 μM ABA or 10 μM Fc to stimulate closure or opening of stomata, respectively. Tissue was mounted onto slides using the nitrate opening buffer and visualized using a Brunel SP300F microscope and images were taken using a MotiCam Pro 252B camera. Geometry measurements were made using the line tool in FIJI. For simulations, stomatal pore area was calculated from mesh data. Meshes were manipulated to capture a paradermal view of the stomatal complex. Images were then thresholded in FIJI and 2D pore area was extracted. Aperture width was measured across the middle of the pore using the line tool in FIJI.

### Computational modelling

Mechanical models were developed in the MorphoMechanX framework (<https://www.morphomechanx.org/>) following the methods previously described.<sup>24,25</sup> The models depend on parameters for the geometry and material properties that are used to model the elastic cell wall. The Finite Element Method (FEM) was used to find the mechanical equilibrium after applying turgor pressure to the walls of the stomatal complex. To obtain the starting geometry for the FEM simulations, surface meshes of stomatal complexes were extracted from 3D confocal images of the ABA-treated stomata using MorphoGraphX,<sup>23</sup> as described in the previous section on confocal imaging and segmentation. A triangular surface mesh was extracted from the segmented image representing the geometry of the cells and cell walls. Each guard and subsidiary cell were closed surfaces made of triangles, with the triangles and vertices shared on the walls between cells. The triangle positions were then used to generate triangular membrane elements, which were assigned a thickness and material parameters. TEM analysis of barley guard cells revealed that the cell wall of the rod region is approximately three times thicker than the cell wall of the bulbous end (Figures 1G, 1H, and S1; Table S1). To capture geometries that were appropriate for simulating the mechanical interactions of GCs, the mesh was derived from fixed samples of either barley or *Brachypodium*. The stomatal complexes of grasses lie in stratified files and showed no change in complex width during opening and closing (Table S3), therefore we fixed the outer boundary of the subsidiary cells in space.

To create a mesh suitable for 3D elements, a slightly coarser triangular mesh of a barley stomate was generated and smoothed to prepare the mesh for extrusion into 3D wedge elements. The smoothing was used to remove artefacts caused by the segmentation process (i.e., kinks and bumps) to prevent the creation of degenerate elements where adjacent faces overlap upon extrusion. Typically, these would occur in regions of high-curvature relative to the extruded thickness. After smoothing, the triangular faces were extruded to generate wedge elements, with the interior surface smoothed to eliminate any remaining overlaps.

The cell walls were modelled as a transverse isotropic Saint-Venant Kirchoff material with two Young's moduli (E1/E3, E2). The Poisson ratios were simplified to a single parameter that approximates the compressibility obtained as if the material was isotropic

(exact in the isotropic case<sup>24</sup>). The Young's modulus,  $E_2$ , defines the material stiffness in the direction of the cellulose microfibril primary orientation (Figures 1K–1M). The other Young's modulus,  $E_1/E_3$ , defines the material stiffness in the orthogonal directions. For simplicity and lack of alternative evidence, we have chosen to adopt the same mechanical parameters for the guard and subsidiary cells.

The pressure of the guard and subsidiary cells are taken from published work<sup>9</sup> where a steady state hydromechanical feedback model<sup>29</sup> was used to estimate guard and subsidiary cell osmotic pressure for a reciprocal pressure model of *Triticum aestivum* (another type of grass guard cell). This model generated guard cell pressures on the order 1.5 to 4.5 MPa and subsidiary cell pressures of 0.2 to 0.7 MPa. A slightly wider range of guard cell pressures was used to match guard cells of other well studied species such as *Arabidopsis thaliana* and *Vicia faba*.<sup>30</sup> The turgor pressure of the cell is applied as a load normal to the triangular elements. Mechanical equilibrium is found using a pseudo time-stepping method, as described.<sup>25</sup>

The template was initialized using the reciprocal pressure model. We set the guard cell pressure at the minimum value of 0.5 MPa and the subsidiary cell pressure at the maximum value, 0.7 MPa, with pressure steps implemented as in Table S2. Young's moduli were chosen so that this initialization step (based on fixed tissue which has lost pressure) approximately matched the pore area of the data for closed, pressurized stomata (Table S3). We then set the pressure of the guard and subsidiary cells and found the mechanical equilibrium of the system.

The output of the model is the deformation, and stress and strain profiles of the stomatal complex, which is dictated by the interplay of stomatal geometry, mechanical parameters, and turgor pressures. From this we can calculate geometrical measurements of the pore such as area, width and length, and measurements of stomatal complex length and width. Stresses and strains are also calculated at the element level, with both using the trace of the respective tensors for visualization.

## QUANTIFICATION AND STATISTICAL ANALYSIS

Most of the experiments comprised at least 20 biological replicates, with the precise sample sizes indicated in the figure legends. Statistical differences were assessed by Students t-test or ANOVA with post-hoc Tukey test, using built-in functions of the statistical package GraphPad, which were also used to assess suitability of the dataset for the test applied. The exact test used is indicated in the figure legends. Statistical difference is indicated on the graphs and in the figure legends. Error bars represent standard error.